

## Structural transformation in nanosized zirconium oxide

M. Jouanne, J. F. Morhange, and M. A. Kanehisa

*Laboratoire des Milieux Désordonnés et Hétérogènes, Unité mixte UPMC-CNRS, UMR7603, Université Pierre et Marie Curie, case 86, 4 Place Jussieu-75252 Paris Cédex 05, France*

E. Haro-Poniatowski, G. A. Fuentes, E. Torres,\* and E. Hernández-Tellez

*División de Ciencias Básicas e Ingeniería Universidad Autónoma Metropolitana Iztapalapa, Apartado Postal 55-534, México 09340, Distrito Federal, Mexico*

(Received 29 December 2000; revised manuscript received 14 May 2001; published 20 September 2001)

Structural properties of calcined  $\text{ZrO}_2$  nanopowders having various sizes were investigated by Raman spectroscopy, x-ray diffraction, and high-resolution transmission electron microscopy. For grain sizes of the order of a few nanometers the Raman spectrum is typical of an amorphous material as is the corresponding x-ray diffractogram. As the size of the grains increases, the spectra progressively evolve towards that of a crystallized sample, furthermore, two regimes of growth, vitreous and crystalline, are evidenced. As opposed to the acoustical, the optical branches exhibit a strong discontinuity near the amorphous-crystalline transition. From the analysis of the Raman spectra as a function of size one can infer the phonon dispersion curves that has so far been inaccessible by neutron diffraction. A simple analysis using a classic elastic model shows that the Raman frequencies of the acoustical phonon bands of the nanograins are linearly dependent upon their size.

DOI: 10.1103/PhysRevB.64.155404

PACS number(s): 78.30-j, 78.67.Bf, 81.05.Je

### I. INTRODUCTION

Raman scattering by confined acoustical phonons in nanoparticles has been studied since the early eighties. It has successfully been applied to small particles of insulators or semiconductors<sup>1-3</sup> where the nanocrystals were embedded in a glassy matrix. Raman scattering of nanoparticles was also observed on  $\text{SiO}_2$  particles in aerogels<sup>4</sup> as well as on metallic nanocrystals embedded in alkali-halide crystals or in glasses.<sup>5-7</sup> Observations of low-frequency bands were reported in various studies of Raman spectra of globular proteins.<sup>8-10</sup> Their occurrence was predicted as early as 1969, together with their interpretation in terms of acoustical vibrations of the proteins.<sup>11,12</sup> It is also interesting to note that similar modes at the other end of the frequency range (fraction of millihertz) are currently studied by geophysicists in very large structures like the Earth.<sup>13,14</sup>

The vibrations of a sphere under stress-free boundary conditions at the surface were first computed by Lamb, more than a century ago.<sup>15</sup> Spheroidal and torsional vibrations were considered. Tamura, Higeta, and Ichinokawa<sup>16,17</sup> and Tamura and Ichinokawa<sup>18</sup> extended that theoretical work by considering different surroundings and thus various boundary conditions for the spheroidal particles. A reasonable agreement is observed between experimental data and the computed mode frequencies given by the above-mentioned theories. Considering the difficulties to describe the boundary conditions when the particles are embedded in a matrix, it is important to test free particles in powder form for which the stress-free boundary conditions of Lamb are valid. To our knowledge, the only reported publication on powders concerns  $\text{TiO}_2$ .<sup>19</sup> The aim of the present work is to investigate the structural properties and the size effects of calibrated nanopowders of  $\text{ZrO}_2$  using their Raman spectra.

Zirconium oxide can be found in three stable phases, cubic (fluorine), tetragonal, and monoclinic. Phase transition temperatures are situated around 2200 °C for the cubic to

tetragonal transitions and near 1100 °C for the tetragonal to monoclinic transition; the latter transition has a width of about 200 °C.<sup>20</sup> The stable phase at ambient temperature is thus monoclinic. However, it is well known that under specific conditions of “wet” preparation, it is possible to obtain a porous polycrystalline metastable zirconia with tetragonal symmetry, stable at ambient and moderate temperatures.<sup>21</sup> By using quenching processes, it is also possible to grow a metastable orthorhombic phase that reverts to monoclinic upon heating above 300 °C or when it is ground in a mortar.<sup>22</sup> A cubic phase can also be made stable at room temperature by mixing zirconia with a few percent of an oxide like  $\text{Y}_2\text{O}_3$ . In addition, amorphous  $\text{ZrO}_2$  can also be prepared. An analysis of the distribution function for the amorphous and the tetragonal phases indicates that they have the same first-neighbors distances, meaning that these phases have a similar short-range order.<sup>23</sup>

The stabilization mechanism of the tetragonal metastable phase at ambient temperature has been the object of numerous discussions for more than 30 years and does not seem to be yet elucidated. The different explanations involve the presence of stabilizing strains,<sup>24</sup> the lower free energy per unit surface of the tetragonal phase versus the monoclinic one,<sup>25,26</sup> the similarity between the amorphous structure and the tetragonal one,<sup>23</sup> and a topotactic crystallization.<sup>27</sup> The relatively large surface area and thus small crystal size of the metastable tetragonal zirconia are a critical factor in its performance as a catalyst in petrochemistry. In fact,  $\text{WO}_x/\text{ZrO}_2$  has been actively studied because of good combination of activity and selectivity in this system.<sup>44</sup>

In this work, a large size range of nanopowders of  $\text{ZrO}_2$  were investigated by Raman spectroscopy, x-ray diffraction, and high-resolution transmission electron microscopy (HRTEM). The combination of these techniques allows to characterize in detail the structural properties of the material as the grain sizes vary.

TABLE I. Diameters of the nanoparticles measured by x-rays and HRTEM for different temperatures of calcination. The size distributions obtained by HRTEM have two peaks for higher calcination temperatures.

Calcination temperature (°C)	Tetragonal size from x rays (nm)	Monoclinic size from x rays (nm)	Size from HRTEM (nm)	
200				
300				
400			5	
500	4.5	1.9	7.5	
600	3.5	3.10	6	12
700	3.00	4.60	10	20
800	2.80	7.80	12	25
900	3.00	13.50		
1000	1.90	16.80		

## II. EXPERIMENT

Our samples of nanometric zirconia ( $ZrO_2$ ) were obtained by hydrolysis of a 0.5 M  $ZrOCl_2$  solution with  $NH_4OH$  (28%) under constant stirring until pH equaled 10. The precipitate was then washed with an aqueous solution of  $NH_4OH$  also at a pH of 10. After that, it was dried in air at 383 K for 15 h and then calcined in air for 1 h. Several different samples were obtained by this procedure upon variation of the calcination temperature. The average crystal-line diameter of the nanoparticles was estimated from the powder x-rays diffraction patterns ( $Cu K_\alpha$  radiation, Ni filter, DRX Siemens mod. D500) using the Scherrer equation with a shape factor of 0.9. Diffraction patterns for the tetragonal metastable phase as well as the monoclinic structures could be observed in many samples. The distribution of the sizes of the nanoparticles was also analyzed by using the images obtained by HRTEM. In most cases a bimodal distribution was observed. Table I summarizes the results for x-rays as well as for the HRTEM measurements. The sizes obtained ranged between 2 and 70 nm, depending on the calcination temperature. It should be noted that, for particle diameters under 5 nm, the size determined by x-rays diffraction can only be indicative.

Raman spectroscopy measurements were performed at room temperature under vacuum ( $10^{-3}$  Torr) in order to suppress the low-frequency Raman signal induced by the rotation modes of the  $N_2$  and  $O_2$  molecules of the ambient air. A Jobin Yvon U1000 double monochromator was used in combination with the 514.5 nm line of an argon laser (Spectra Physics) at a power level of 5 mW focused onto a 100  $\mu m$  diameter spot. Raman spectra were taken directly from zirconia powder freely deposited on microscope slides as well as from pellets crushed under moderate pressure. Similar spectra were obtained in both cases.

To recover the true line shape of the modes, all spectra are reduced by the Bose-Einstein factor and put in the form

$$I(\omega) = \left[ n \left( \frac{\hbar \omega}{kT} \right) + 1 \right] R(\omega). \quad (1)$$

Here, we take the spectral function  $R(\omega)$  as the imaginary part of the retarded-phonon Green's function of the form<sup>30</sup>

$$R(\omega) = \text{Im} \left\{ \frac{A}{(\omega + i\Gamma)^2 - \omega_0^2} \right\} = \frac{2A\omega\Gamma}{(\omega^2 - \omega_0^2 - \Gamma^2)^2 + 4\omega^2\Gamma^2}, \quad (2)$$

where  $\text{Im}\{ \}$  means the imaginary part,  $\omega_0$  is the mode frequency,  $A$  the oscillator strength, and  $\Gamma$  is the width. This formula coincides with the usual damped oscillator response function<sup>29</sup> if one makes the substitution:

$$\omega_0^2 + \Gamma^2 \rightarrow \omega_0^2, \quad 2\Gamma \rightarrow \Gamma.$$

Because of the symmetry property of the Bose-Einstein function [ $n(-x) + 1 = -n(x)$ ] and odd parity of  $R(\omega)$ , Eqs. (1) describes the Stokes domain as well as the anti-Stokes one. While the line shape described by Eqs. (2) is similar to usual Lorentzian peak when  $\omega_0$  is large and  $\Gamma$  is small, it is no longer the case when the scattered light frequency is situated in the vicinity of the Rayleigh line. Note that  $\omega_0$  is not exactly the apparent frequency of the maximum of the peak and  $\Gamma$  is not its apparent half-width either. Finally it is to be noted that the true line shape of the weak low-frequency modes can be recovered only when the entire spectrum including strong nearby high frequencies features are fitted simultaneously.

A small and broad luminescence background was usually observed just after the initial laser irradiation. A similar broadband has been observed on zirconia subjected to a UV excitation<sup>31</sup> and is different from the sharp luminescence peaks also observed at lower energy.<sup>32</sup> The intensity of this band decreases during the irradiation and stabilizes after a few tens of hours at the specified power density. The residual band was subtracted from the spectra and the quality of the subtraction was accurately controlled by checking the symmetry of the Stokes and anti-Stokes parts of the spectra after reduction by the Bose-Einstein factor.

## III. RESULTS AND DISCUSSION

### A. High-resolution transmission electron microscopy results

High-resolution transmission electron microscopy images of some calcined powders are shown in Fig. 1. At 300 °C [Fig. 1(a)] no reticular planes can be observed indicating that the sample is still amorphous. As the calcination temperature grows, these planes are clearly observed. Furthermore, one can roughly estimate the size of the nanograins from the micrographs as it is shown in Figs. 1(b), 1(c), and 1(d).

### B. X-ray diffraction results

Figure 2 presents diffractograms, taken at ambient temperature, for some samples annealed at various temperatures. All the diffraction bands observed can be assigned to the monoclinic phase with the exception of one band centered near 30° that is typical of the tetragonal phase. To extract the widths of the diffracted bands, a least squares best fit with three Lorentzian profiles was performed on the two largest bands of the monoclinic phase (near 28.2° and 31.4°) and the single band related to the tetragonal phase at 30°. Broadening by the diffractometer was roughly taken into account by deconvoluting the measured widths using the equation  $W_d$

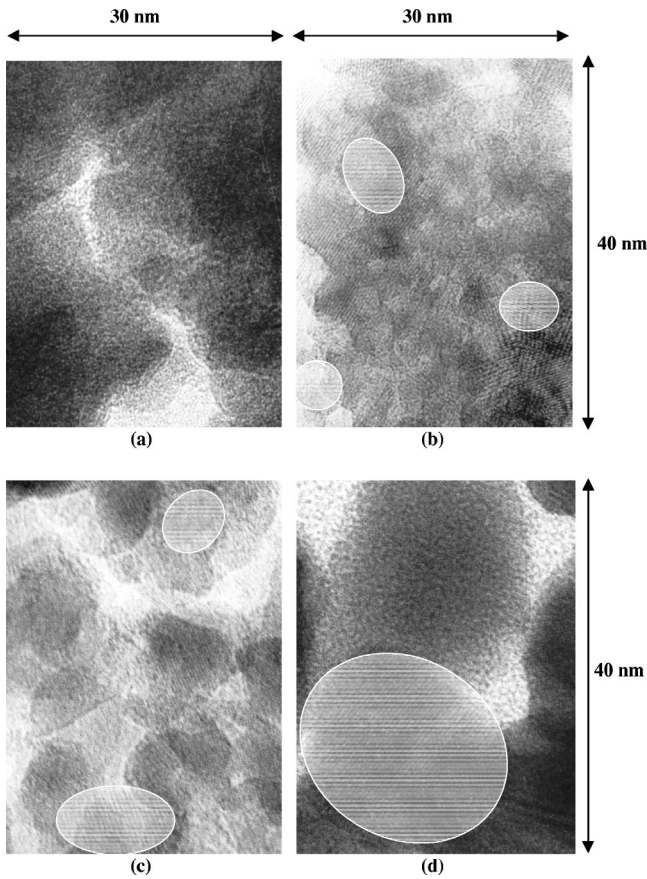


FIG. 1. HRTEM image of a  $ZrO_2$  in powder form calcined at (a) 300 °C, (b) 500 °C, (c) 600 °C, and (d) 700 °C. For higher temperatures, reticular planes (marked) of larger sizes are observed.

$= \sqrt{W_{ob}^2 - X^2}$ , where  $W_{ob}$  is the observed width of the Lorentzian,  $W_d$  its deconvoluted width, and  $X$  the “apparatus width” approximated by the observed width for a sample annealed at 1000 °C for which the size of the crystallites is much larger than for the samples annealed below 800 °C.

These best fits are plotted as continuous lines on Fig. 2. From the fitted widths of the diffracted patterns, the mean size of the nanostructures were determined using the Scherrer equation as noted above. The measured size of the metastable tetragonal phase of zirconia is nearly constant (around 5 nm) for all the annealing temperatures where this phase can

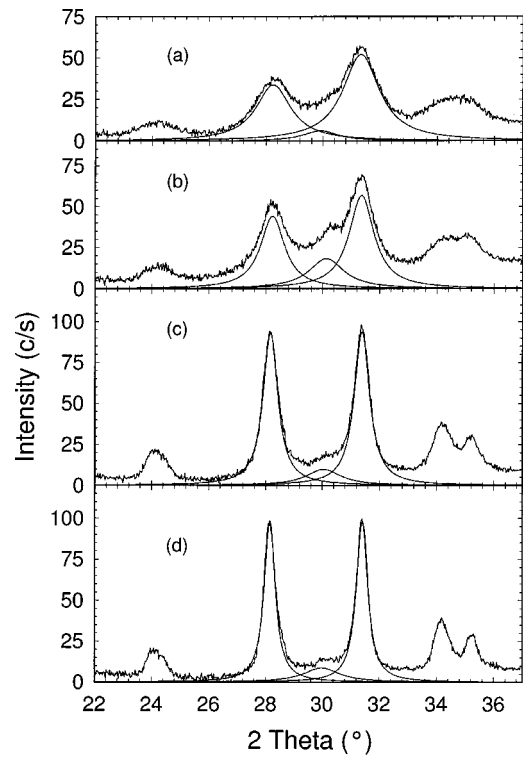


FIG. 2. X-ray diffractograms of the samples annealed at (a) 400 °C, (b) 500 °C, (c) 700 °C, and (d) 800 °C, respectively. The continuous lines represent least square best fits to a sum of Lorentzian functions. We see an increase in crystallinity as the calcination temperatures are raised.

be observed (400–1000 °C). The dependence of the measured size for the monoclinic phase is shown on Fig. 3, where the logarithm of the reduced sizes is plotted against the inverse calcination temperature. The reduced size is defined as  $D/2a$ , ratio of the measured sizes  $D$  by twice the mean lattice parameter  $(a_1 + a_2 + a_3)/3$  of the monoclinic  $ZrO_2$ . Two different regimes are clearly distinguished on this figure. To describe this behavior, the following function was then fitted to the data points:

$$D(T) = D_0 e^{-E_a(T)/T}, \tag{3}$$

where

$$\frac{E_a(T)}{T} = \frac{(E_{a1} + E_{a2}) \left( \frac{1}{T} - \frac{1}{T_0} \right) - \left\{ \left[ (E_{a1} - E_{a2}) \left( \frac{1}{T} - \frac{1}{T_0} \right) \right]^2 + 4\Delta^2 \right\}^{1/2}}{2}. \tag{4}$$

The latter form was chosen so that the argument of the exponential in Eq. (3) is a hyperbola in  $1/T$  having, as asymptotes, two lines of slopes  $E_{a1}$  and  $E_{a2}$ . The  $E_{a1}$  and  $E_{a2}$  slopes are energy parameters describing the crystalline and vitreous regimes, respectively.  $E_{a2}$  is smaller than  $E_{a1}$ , cor-

responding to the fact that it costs less energy for particles to diffuse in vitreous phase. The formula (4) thus represents the cross over from amorphous regime to the crystalline one. The two other parameters  $T_0$  and  $\Delta$  represent respectively the temperature and the width of the transition, a small

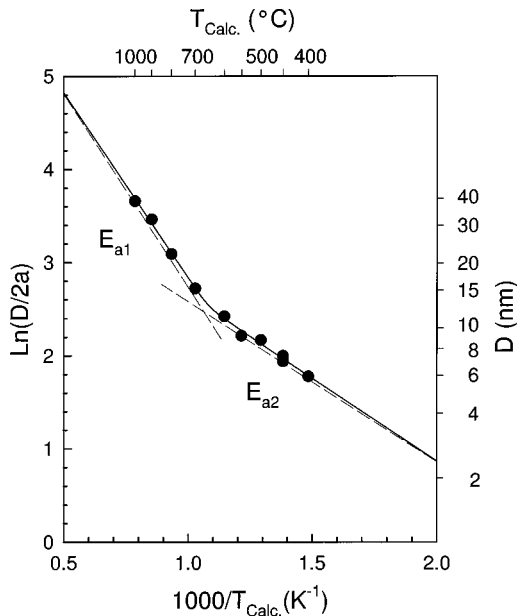


FIG. 3. Logarithm of the reduced size of the nanoparticles as a function of the inverse calcination temperature. The dotted and straight lines represent least square best fits to the experimental data. We distinguish clearly two regimes of growth, crystalline and vitreous, characterized by two activation energies,  $E_{a1}$  and  $E_{a2}$ , respectively. The transition between these two regimes are rather abrupt and takes place at about  $T=650$  °C.

$\Delta(\Delta \ll 1)$  corresponding to an abrupt transition. By least square fitting, we obtain the crystalline and vitreous characteristic energies  $E_{a1}=0.343$  eV,  $E_{a2}=0.153$  eV and the two other parameters  $T_0=652$  °C and  $\Delta=0.0377$ . This last parameter gives a rather abrupt transition, showing that the two regimes are well separated by a narrow range of temperatures.

### C. Raman results

Figure 4 presents the reduced Raman spectra of different samples, annealed at various calcination temperatures. For calcination temperatures ( $T_c$ ) lower than 310 °C, the Raman spectrum is composed of broad bands centered at 310 and 550  $\text{cm}^{-1}$  [Fig. 4(a)]. This spectrum is typical of an amorphous material and reflects its phonon density of states. The amorphous character is confirmed by the corresponding HRTEM images obtained on the samples calcined at temperature below 300 °C where it is not possible to observe any lattice structure [see Fig. 1(a)]. Around 360 °C [Fig. 4(b)], at frequencies larger than 80  $\text{cm}^{-1}$ , seven large bands are observed near 96, 185, 335, 380, 478, 550, and 620  $\text{cm}^{-1}$ . These bands are characteristic of the tetragonal phase of zirconia.<sup>33,34</sup> Furthermore, the band centered at 185  $\text{cm}^{-1}$  in this spectrum already begins to split into two peaks. As the temperature increases, there is a progressive splitting of the bands associated with the appearance and growth of monoclinic phase. The bands at 185, 335, and 620  $\text{cm}^{-1}$  split into bands located at 178.5–191, 332–347, and 615–638  $\text{cm}^{-1}$ , respectively, as shown in Figs. 4(c)–4(e). At the same time, the remaining bands at 96, 380, and 478  $\text{cm}^{-1}$  shift and

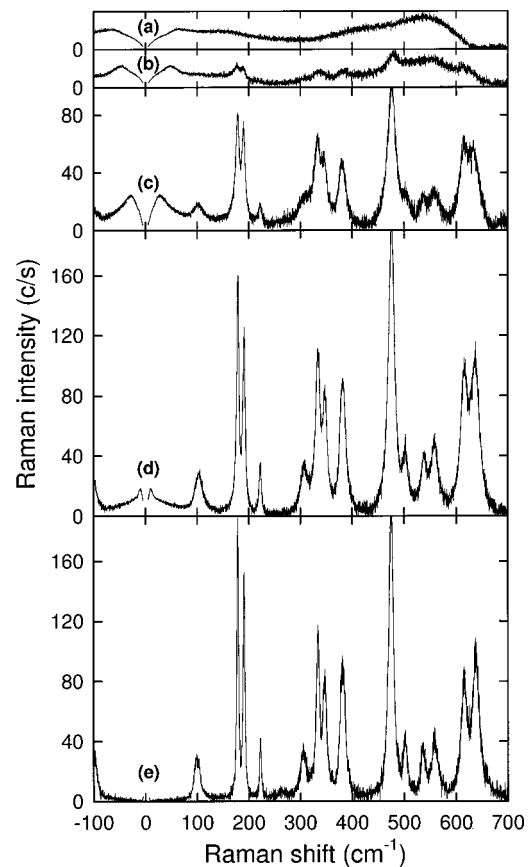


FIG. 4. Raman spectra of the nanopowders annealed at (a) 250 °C, (b) 360 °C, (c) 500 °C, (d) 700 °C, and (e) 1000 °C, respectively. We observe evolution of amorphous phases [(a), (b)] to crystalline phase [(c)–(e)].

sharpen, pointing at 100, 381, and 475  $\text{cm}^{-1}$  and new peaks appear at 223, 315, 536, 558, and 750  $\text{cm}^{-1}$ . Spectrum 3e of the 1000 °C calcined  $\text{ZrO}_2$  is similar to the spectra previously reported for the monoclinic phase of zirconia.<sup>35</sup> For this phase (space group  $C_{2h5}$ ), 18 modes are expected to be Raman active, most of which are effectively observed. While the frequency shift of the peaks is primarily due to the increasing size of the  $\text{ZrO}_2$  crystallites,<sup>36</sup> the mixture of the metastable tetragonal phase with the monoclinic phase obscures the effect. It is thus difficult to extract information concerning the size of the nanocrystals from the optical phonon domain of the Raman spectrum.

An expanded view of the frequency region under 200  $\text{cm}^{-1}$  is shown on Fig. 5 that presents the Raman spectra of the powders for different calcination temperatures. As it is obvious on this figure, the low-frequency feature (under 80  $\text{cm}^{-1}$ ) can be decomposed into two broad bands. When the temperature of calcination increases, these two bands shift towards lower frequencies. As was stated in Introduction, this behavior has already been observed in many systems of nanoparticles of increasing size embedded in various matrices and interpreted in terms of confined acoustical vibrational modes.<sup>1–7</sup> In the present case the size of the nanoparticles grows as the calcination temperature increases as shown in Table I. To analyze the experimental data below

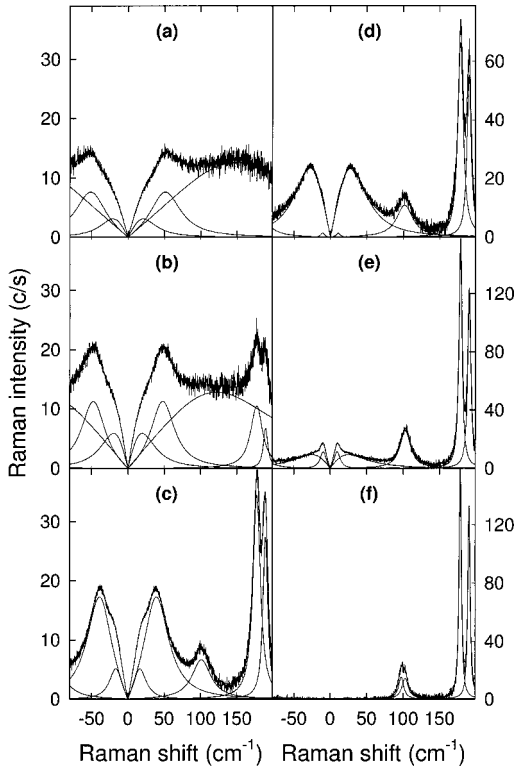


FIG. 5. Extended low-frequency Raman spectra of the samples annealed at (a) 330 °C, (b) 360 °C, (c) 400 °C, (d) 500 °C, (e) 700 °C, (f) 1000 °C, respectively. The solid lines represent the least square best fits with functions given by Eq. (2). We observe that the low-frequency feature ( $<80 \text{ cm}^{-1}$ ) is composed of two bands and shifts toward low frequency when the calcination temperature increases.

$250 \text{ cm}^{-1}$ , the reduced spectra were fitted to a sum of six damped oscillators of the shape given in Eq. (2). For all the samples, the frequencies of all the oscillators deduced from this fit as well as the frequencies of the peaks situated above  $250 \text{ cm}^{-1}$  are plotted in Fig. 6 as a function of the inverse of the reduced size as defined above ( $2a/D$ ). For the lowest calcination temperatures (200, 250, and 300 °C), because of the amorphous nature of the sample, broad peaks are only observable making it impossible to extract a size information from the x-rays diffractograms. The corresponding size values were obtained by extrapolation on the fit of the low-temperature regime of Fig. 3. At the calcination temperature  $T_c = 310 \text{ °C}$  we find a discontinuity in all the optical modes, while the acoustic modes change continuously. This means that the frequencies of acoustic modes are uniquely determined by the grain size. Figure 6 can also be regarded as the phonon dispersion curve of monoclinic  $\text{ZrO}_2$ . In fact, in superlattices, it is well known that confined modes frequencies for a layer of thickness  $h$  is approximated by the bulk phonon frequency of wave vector  $k = \pi/h$ ,<sup>37</sup> and one can even reconstruct the phonon dispersion curves from the superlattice modes measurements.<sup>38</sup> Phonon dispersion curve of  $\text{ZrO}_2$  is experimentally only available for the acoustic modes in the bulk cubic stabilized phase<sup>39,40</sup> and thus Fig. 6 can be considered as the first dispersion curve of monoclinic  $\text{ZrO}_2$  for the whole branches, except for higher  $k$  values of the optical modes.

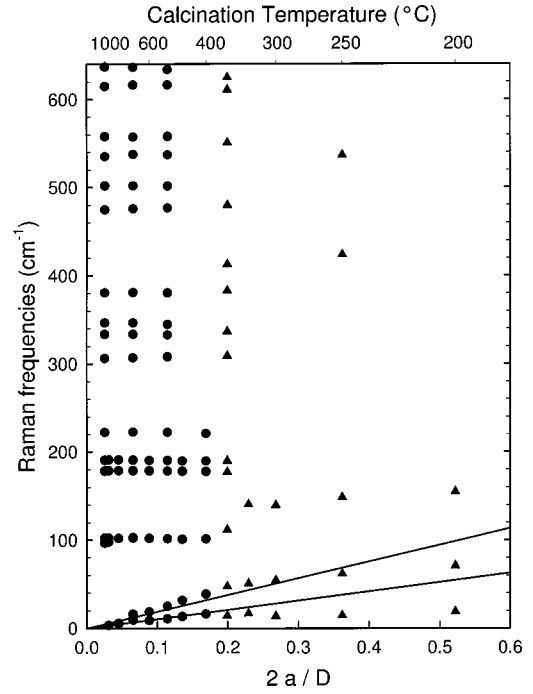


FIG. 6. Raman frequencies as a function of the inverse reduced size of nanoparticles. The two straight lines represent the calculations using Eq. (5). Triangles correspond to sample whose nanoparticle sizes were not measured but determined by extrapolation on Fig. 3. This figure can also be considered as the phonon dispersion for monoclinic  $\text{ZrO}_2$  (see text).

#### D. Discussion

As observed in Fig. 1(a), around 300 °C the  $\text{ZrO}_2$  nanopowder is amorphous. In fact, the first nanocrystals can be detected by x-ray diffraction and Raman spectroscopy near 360 °C. Below this temperature, information about the size of nanoparticles can only be extracted from Fig. 3 as described in the preceding paragraph. A so-called crystallization exotherm is known to occur around 460 °C while synthesizing zirconia.<sup>21,41</sup> The exotherm shifts in temperature and varies in intensity depending on the purity of the sample and on experimental conditions. Our results show that the Raman frequencies become stable at about that temperature (see for example the band at  $96 \text{ cm}^{-1}$  in Fig. 6). It is also interesting to note that there is coexistence of phases (monoclinic and tetragonal) up to about 600 °C as revealed by x-rays diffraction (Fig. 2) and Raman spectroscopy (Figs. 4 and 6).

Concerning the low-frequency region of the Raman spectra, we have compared the experimental values of the  $\omega_{0i}$  deduced from the fit to a calculation of the frequencies of the first two Raman-active modes<sup>42</sup> of nanoparticles modeled as spheres. The frequencies of these modes are inversely proportional to their radius, according to the expression

$$\sigma = \left( \frac{X}{\pi} \right) \frac{V_t}{30 D}, \quad (5)$$

where  $V_t$  is the transverse velocity of sound in m/s.  $D$  the diameter or the particle in nanometer, and  $X$  a numerical

constant depending upon the sound velocities and the mode index.<sup>15</sup> To achieve this calculation, the value of the sound velocities (longitudinal and transverse) of the material is required. We have used the elastic constants extrapolated for zero-porosity monoclinic polycrystalline ZrO<sub>2</sub> given in Ref. 43:

$$E = 2.44 \times 10^{12} \text{ dyne/cm}^2 \quad (\text{Young's modulus}),$$

$$\mu = 0.97 \times 10^{12} \text{ dyne/cm}^2.$$

Computing the other Lamé constant  $\lambda = \mu(E - 2\mu)/(3\mu - E) = 1.03 \times 10^{12} \text{ dyne/cm}^2$  and using the zero-porosity density of  $5.71 \text{ g/cm}^3$  of Ref. 43, we obtain for the longitudinal and transverse sound velocities:

$$V_l = \left( \frac{\lambda + 2\mu}{\rho} \right)^{1/2} = 7212 \text{ m/s},$$

$$V_t = \left( \frac{\mu}{\rho} \right)^{1/2} = 4122 \text{ m/s}.$$

These values have been used for the three phases of ZrO<sub>2</sub> involved in the range of temperature where the two low-frequency modes are observed.

The straight lines of the calculated frequencies versus the inverse of the radius for the two possible Raman-active fundamental spheroidal modes  $l=0$  and  $l=2$ , (the  $l=2$  of torsional mode being Raman forbidden) are plotted in Fig. 6, using these sound velocities. A reasonable fit is observed between the lines and the experimental points for the largest grain sizes, considering the crude approximation on the sound velocities and the nonspherical shape of the nanoparticles. For the smallest sizes (low calcination temperatures), the agreement is poorer as one would expect since the ap-

proximation of the elastic properties of continuous media used for the calculations is no longer valid. This behavior is similar to the bending of the acoustical branches of the dispersion curves for large wave vectors and has already been observed in the case of bismuth nanoparticles embedded in amorphous germanium.<sup>44</sup>

#### IV. CONCLUSION

This work is a systematic study on free nanograins of ZrO<sub>2</sub> over a wide range of sizes, obtained using several complementary experimental tools: x-ray diffraction, high-resolution transmission electronic microscopy, and Raman spectroscopy. The Raman spectra are found to be strongly dependent on the crystallinity, phase, and size of the nanoparticles. As usual, the Raman optical frequency range allows a clear distinction between the amorphous and the crystalline phases. In the low-frequency range of the Raman spectra, a good agreement between the frequencies of the confined acoustical phonon bands and the frequencies given by a simple elastic model describing the vibrations of a spherical nanoparticle is obtained. We have established the distinction of growth regimes for amorphous and crystalline phases and its crossover at about  $T = 650 \text{ }^\circ\text{C}$ . We have succeeded in reconstructing the phonon dispersion curve for bulk monoclinic ZrO<sub>2</sub>, for which no neutrons data are available.

#### ACKNOWLEDGMENTS

The present work was financed by a CNRS-CONACYT collaboration project #E130.1868/2000 and a CONACYT grant #400200-5-C039-A. One of us (E.H.E.) thanks the Universidad Autonoma Metropolitana Iztapalapa for their support during sabbatical leave.

\*Permanent address: Instituto de Materiales y Reactivos (IMRE) Facultad de Química, Universidad de la Habana, Zapata y G. Vedado, Ciudad de la Habana 10400, Cuba.

<sup>1</sup>B. Champagnon, A. Boukenter, E. Duval, C. Mai, G. Vigier, and E. Rodek, *J. Cryst. Solids* **94**, 216 (1987).

<sup>2</sup>B. Champagnon, B. Andrianasolo, and E. Duval, *Mater. Sci. Eng.*, **B 9**, 417 (1991).

<sup>3</sup>M. Fujii, Y. Kanzawa, S. Hayashi, and K. Yamamoto, *Phys. Rev. B* **54**, R8373 (1996).

<sup>4</sup>A. Boukenter, B. Champagnon, E. Duval, J. L. Rousset, J. Dumas, and J. Serughetti, *J. Phys. C* **21**, L1097 (1988).

<sup>5</sup>G. Mariotto, M. Montagna, G. Viliani, E. Duval, S. Lefrant, E. Rezpka, and C. Mai, *Europhys. Lett.* **6**, 239 (1988).

<sup>6</sup>M. Fujii, T. Nagareda, S. Hayashi, and K. Yamamoto, *Phys. Rev. B* **44**, 6243 (1991).

<sup>7</sup>M. Fujii, T. Nagareda, S. Hayashi, and K. Yamamoto, *J. Phys. Soc. Jpn.* **61**, 754 (1992).

<sup>8</sup>W. L. Peticolas, *Methods in Enzymology* (Academic, New York, 1979), Vol. 61, Enzyme Structure, Part H, p. 425.

<sup>9</sup>P. C. Painter, L. E. Mosher, and C. Rhoads, *Biopolymers* **21**, 1469 (1982).

<sup>10</sup>M. Picquart, E. Haro-Poniatowski, J. F. Morhange, M. Jouanne, and M. Kanehisa, *Biopolymers* **53**, 342 (2000).

<sup>11</sup>P. G. de Gennes and M. Papoular, *Polarisation, Matière et Rayonnement. Volume in Honor of Alfred Kastler* (Presses Universitaires de France, Paris, 1969), p. 243.

<sup>12</sup>Y. Suezaki and N. Go, *J. Pept. Protein Res.* **7**, 333 (1975).

<sup>13</sup>P. Lognonné, *J. Geophys. Res.* **96**, 2309 (1991).

<sup>14</sup>T. Tanimoto, J. Um, K. Nishida, and N. Kobayashi, *Geophys. Res. Lett.* **25**, 1553 (1998).

<sup>15</sup>H. Lamb, *Proc. London Math. Soc.* **13**, 189 (1882).

<sup>16</sup>A. Tamura, K. Higeta, and T. Ichinokawa, *J. Phys. C* **15**, 4975 (1982).

<sup>17</sup>A. Tamura, K. Higeta, and T. J. Ichinokawa, *J. Phys. C* **16**, 1585 (1983).

<sup>18</sup>A. Tamura and T. Ichinokawa, *J. Phys. C* **16**, 4779 (1983).

<sup>19</sup>M. Gotic, M. Ivanda, S. Popovic, S. Music, A. Sekulić, A. Turkovic, and K. Furic, *J. Raman Spectrosc.* **28**, 555 (1997).

<sup>20</sup>K. Negita and H. Takao, *J. Phys. Chem. Solids* **50**, 325 (1989).

<sup>21</sup>P. D. L. Mercera, J. G. van Ommen, E. B. M. Doesburg, A. J. Burgraaf, and J. R. H. Ross, *Appl. Catal.* **57**, 127 (1990).

<sup>22</sup>R. Suyama, R. Ashida, and S. Kume, *J. Am. Ceram. Soc.* **68**, C-314 (1985).

<sup>23</sup>J. Livage, K. Doi, and C. Mazieres, *J. Am. Ceram. Soc.* **51**, 349 (1968).

<sup>24</sup>T. Mitsuhashi, M. Ichibara, and U. Tatsuke, *J. Am. Ceram. Soc.* **57**, 97 (1974).

- <sup>25</sup>R. C. Garvie, *J. Phys. Chem.* **82**, 1238 (1978).
- <sup>26</sup>R. C. Garvie and M. F. Goss, *J. Mater. Res. Sci.* **21**, 1253 (1986).
- <sup>27</sup>E. Tani, M. Yoshimura, and S. Somiya, *J. Am. Ceram. Soc.* **66**, 11 (1983).
- <sup>28</sup>D. G. Barton, S. L. Soled, G. D. Meitzner, G. A. Fuentes, and E. Iglesia, *J. Catal.* **181**, 57 (1999).
- <sup>29</sup>A. S. Barker, Jr. and R. Loudon, *Rev. Mod. Phys.* **44**, 18 (1972).
- <sup>30</sup>A. A. Abrikosov, L. P. Gor'kov, and I. Y. Dzyaloshinskii, *Quantum Field Theoretical Methods in Statistical Physics* (Pergamon, Oxford, 1965).
- <sup>31</sup>J. F. Sarver, *J. Electrochem. Soc.* **113**, 124 (1966).
- <sup>32</sup>I. M. Asher, B. Papanicolaou, and E. Anastassakis, *J. Phys. Chem. Solids* **37**, 221 (1976).
- <sup>33</sup>E. Anastassakis, B. Papanicolaou, and I. M. Asher, *J. Phys. Chem. Solids* **36**, 667 (1975).
- <sup>34</sup>A. Feinberg and C. H. Perry, *J. Phys. Chem. Solids* **42**, 513 (1981).
- <sup>35</sup>V. G. Keramidis, W. B. White, *J. Am. Ceram. Soc.* **57**, 22 (1974).
- <sup>36</sup>L. Fangxin, Y. Jinlong, and Z. Tianpeng, *Phys. Rev. B* **55**, 8847 (1997).
- <sup>37</sup>A. K. Sood, J. Menendez, M. Cardona, and K. Ploog, *Phys. Rev. Lett.* **54**, 2111 (1985).
- <sup>38</sup>B. Jusserand and M. Cardona, in *Light Scattering in Solides V. Superlattices and Other Microstructures*, edited by M. Cardona and G. Güntherodt (Springer, Berlin, 1988), p. 49.
- <sup>39</sup>D. W. Liu, C. H. Perry, A. A. Feinberg, and R. Currat, *Phys. Rev. B* **36**, 9212 (1987).
- <sup>40</sup>D. N. Argyriou, M. M. Elcombe, and A. C. Larson, *J. Phys. Chem. Solids* **57**, 183 (1996).
- <sup>41</sup>E. Torres-Garcia, C. Vasquez-Ramos, A. Peláiz-Barranco, and G. A. Fuentes (unpublished).
- <sup>42</sup>E. Duval, *Phys. Rev. B* **46**, 5795 (1992).
- <sup>43</sup>C. F. Smith and W. B. Crandall, *J. Am. Ceram. Soc.* **47**, 624 (1964).
- <sup>44</sup>E. Haro-Poniatowski, M. Jouanne, J. F. Morhange, M. Kanehisa, R. Serna, and C. N. Afonso, *Phys. Rev. B* **60**, 10 080 (1999).